Li interaction-induced phase transition from black to blue phosphorene

Md Rajib Khan Musa, Congyan Zhang, Manthila Rajapakse, Jacek B. Jasinski, Gamini Sumanasekera, and Ming Yu

Phys. Rev. Materials **5**, 024007 — Published 22 February 2021

DOI: 10.1103/PhysRevMaterials.5.024007

Li Interaction-Induced Phase Transition from Black to Blue Phosphorene

Md Rajib Khan Musa[a], Congyan Zhang[a†], Manthila Rajapakse[a], Jacek B. Jasinski[b], Gamini Sumanasekera[a,b], and Ming Yu[a*]

[a]*Department of Physics & Astronomy, University of Louisville, Louisville, KY, 40292, USA*

[b]*Conn Center for Renewable Energy Research, University of Louisville, Louisville, KY, 40292, USA*

PACS: 61.43.Bn, 61.46.−w, 64.60.A−, 64.70.Nd

Corresponding Author

* Ming Yu, m0yu0001@louisville.edu, Phone: (502) 852-0931

ORCID: Ming Yu 0000-0002-4041-5177

Present Addresses

† Congyan Zhang: Southern University and A&M College, Baton Rouge, LA, 70813

ABSTRACT: A comprehensive first-principle calculation has been carried out and revealed that at sufficiently high Li concentration and certain well-defined configurations a phase transition from black to blue phosphorene can take place. Blue phosphorene, a newly predicted allotrope of phosphorus, possesses unique crystalline and electronic structure and is a promising candidate, not only for fundamental research but also for electronic and optoelectronic applications. Methods to growth high quality blue phosphorene layers are highly desirable but challenging. Here, a novel kinetic pathway to grow blue phosphorene layers from black phosphorene layers via Li intercalation is proposed based on first principle study. This study pointed out that Li atoms intercalated in black phosphorene could act as 'catalyst' in the 'reactive region' of the lone

pair of P atoms, leading to a P-P bond breaking and subsequently, a local structural transformation from orthorhombic lattice to an assembly of parallel narrow nanoribbons with rhombohedra-like symmetry. During Li deintercalation, these nanoribbons are self-mended and form blue phosphorene layers. The interlayer distance was found 4.60 Å for double layer with AA stacking and 4.13 Å for multilayer with ABC stacking, respectively, indicating a monolayer blue phosphorene can be mechanically exfoliated. This study also points out the possibility of new phases in other systems, where intercalation can lead to an unexpected structural phase transition and even a discovery of novel materials.

I. INTRODUCTION

Since the discovery of graphene in 2004 [1], there has been a quest for new two-dimensional (2D) materials aimed at exploring new fundamental phenomena stemming from quantum confinement and size effects. This quest has spurred new areas of research with rapid growth from both theoretical and experimental fronts aimed at fundamental science and technological advancements. 2D materials also provide the opportunity for new concepts for the next generation electronic and nanoscale devices. They tend to have excellent mechanical properties [2] and can be prepared and transferred to arbitrary substrates making them mechanically compatible with flexible device fabrication. At the same time, the transport properties of 2D materials [3], when grown over large areas by chemical vapor deposition (CVD) and consisting of large single crystalline domains, can be orders of magnitude higher than for materials used at present, such as organic semiconductors [4], thus enabling higher frequency applications at low power. Further, the photo-carrier lifetime can be considerably prolonged due to charge separation

promoted by surface states [5]. The strong light absorption in 2D materials is attributed to high density of states [6].

Among recently discovered 2D materials, black phosphorene, a monolayer of black phosphorus (BP) has been attracting attention because of its anisotropic properties and numerous foreseeable applications [7]. Due to the sp^3 hybridization, phosphorene does not form atomically flat sheets like graphene but a puckered honeycomb-structured layer [8, 9]. Recent reports have brought to light the highly encouraging prospects of using this novel 2D material in both electronic and optoelectronics. The key characteristics that make it so promising are high carrier mobility (~286 $cm^2V^{-1}s^{-1}$), strong in-plane anisotropy, particularly the anisotropy of electric conductance, and highly tunable band gap, which changes with doping, functionalization, and the number of layers (*e.g.*, the measured optical gap from ~1.9 eV for a monolayer to 0.3 eV for bulk black phosphorus [10]). The on/off ratio and the carrier mobility are also layer-dependent [11]. Furthermore, compatibility of phosphorene with other 2D materials in so-called van der Waals heterostructures can offer solutions for important issues, such as surface degradation, doping, or control of surface/interface electronic structure, and can also enable novel functionalities and devices with unique or unprecedented performance.

Soon after the discovery of black phosphorene [12, 13], blue phosphorene, the new member of 2D material in phosphorus family, has been theoretically proposed [14]. Structurally, it has slightly flatter "zigzag" ridges other than the deeper "armchair" ridges of black phosphorene. Energetically, blue phosphorene is nearly as stable as BP allotrope (with the binding energy difference < 2 meV/atom) [14, 15]. Electronically, it has even a wide fundamental band gap (> 2 eV) compared to black phosphorene, tunable gap depending on the number of layers,

semiconducting-semimetal transition under strain, possible high carrier mobility, and higher in-plane rigidity, which makes it a promising candidate in the emerging field of post-graphene 2D electronics [14]. Layered blue phosphorene also exhibits superconductivity with metal intercalations [16]. Blue phosphorene nanoribbons show their anisotropic quantum confinement nature on the bandgap [17]. Their electronic band structure and magnetic properties can be controlled by means of passivation [18, 19]. The blue phosphorene oxide, on the other hand, offers an intriguing platform for the exploration of fundamental properties of quantum phase transitions and novel emergent fermions [20].

For future device applications, it is highly desirable to develop efficient fabrication methods for mass production of high-quality blue phosphorene. Recently, methods for the direct growth of single-layered blue phosphorene via epitaxial growth on a proper catalytic substrate (*e.g.* tellurium functionalized Au(111), Cu(111), and GaN, *etc*.) by using BP as the precursor have been developed [21-23] or proposed [24]. It was found that the blue phosphorus layer weakly interacts with the substrate and a quasi-free-standing single layer blue phosphorus might be obtained. The size of the rhombus structure and the quality of single layer blue phosphorus were found depending on the choice of substrates (due to the lattice mismatch and binding energy between blue phosphorene and substrates) [21, 22]. Mechanical exfoliation from blue phosphorus, on the other hand, is a possible pathway to a direct growth of blue phosphorene. However, direct exfoliation from blue phosphorus still remains a challenge since blue phosphorus can only exists at high pressure (> 5 GPa) [25-27] and the blue phosphorus converts back to black phosphorus accompanied with the release of pressure [28]. Therefore, to date, direct growth of freestanding blue phosphorene remains a daunting challenge and seeking other possible pathway to obtain blue phosphorene is desired.

The crystalline structure of BP consists of armchair-ridge-puckering structure and rings of three-connected P atoms in chair conformation sharing edges like in cis-decalin [15]. The blue phosphorus, on the other hand, exhibits an arsenic-type (rhombohedral) structure, made of layers of six-membered rings linked in trans-decalin fashion. They can be accommodated in a common monoclinic subgroup (P2/c) with P atoms on general Wyckoff positions (4g) [15]. Under moderate compression (~ 5GPa), lone pair electrons are squeezed out of interlayer van der Waals reservoir into the P-P bond scaffolding, and leads to a formation of a Peierls intermediate along the transformation from black to blue phosphorus [15]. Such atomistic mechanism provides a hint to find alternative possible pathway in synthesizing blue phosphorene. For instance, instead of using pressure, one might consider incorporating foreign elements, such as Li, to induce the structural phase transition from black to blue phosphorus so that mechanical exfoliation become technically feasible.

Intercalation has become one of the most widely used techniques to modify properties of 2D materials and has been applied as a mean of exfoliating individual 2D layers from their bulk counterparts in large quantities [29, 30]. However, whether it can be effectively applied to induce phase transitions and the accompanying fundamental mechanism are not clear. Here, by applying first-principles approaches, we proposed to explore whether Li intercalation could induce the transition from black to blue phosphorus so that mechanical exfoliation become technically feasible and to reveal the atomistic mechanism of Li mediated phase transition from black to blue phosphorus. We found that the fundamental mechanism of the bond-to-lone pair interconversion from black to blue phosphorus mediated by the pressure [15] can also be realized via Li intercalation. In particular, we found that Li atoms could act as ‘catalyst’ that guides the structural transition. We identified the conditions for the Li distribution during intercalation and

provided a fundamental guideline for synthesis of high-quality large size of blue phosphorene. Our study prompts the idea that Li intercalation can drive the P atoms moving along specific directions, resulting in bond breaking and reforming, and subsequently reducing the energy barriers for structural phase transitions. This offers new pathways for the synthesis of blue phosphorene and creates an opportunity to explore novel physical phenomena in this and similar 2D systems.

II. COMPUTATIONAL METHOD

We performed a systematic first principle calculations based on the density functional theory (DFT) [31, 32], implemented in the Vienna Ab-initio Simulation Package (VASP) [32]. The core-valence interaction was described by the frozen-core projector augmented wave (PAW) method [34] (*i.e*., considering one (*s*) valence electron on Li and five (two *s* and three *p*) valence electrons on P atoms, respectively). The generalized gradient approximation (GGA) [35] of Perdew-Burke-Ernzerhof (GGA-PBE) [36] was adopted for exchange-correlation functional. For the study of Li intercalation on monolayer and double layer black phosphorene, a 2x2 planar supercell was chosen with a vertical vacuum space of 25 Å between adjacent layers to avoid any mirror interactions. For the study of Li intercalation in the black phosphorus, an orthorhombic unit cell was chosen. The Brillouin zone was sampled either by 16x1x12 (for single and double layered systems) or by 9x9x9 (for multilayered systems) gamma-centered *k*-point meshes generated in accordance with the Monkhorst-Pack scheme [37] in the structural relaxation and charge distribution calculations. An energy cutoff of 300 eV was set for the plane wave basis in all calculations. Energy and force convergence criteria were set to be 10^{-4} eV and 10^{-3} eV/Å, respectively. The systems were fully relaxed using Conjugate-Gradient algorithm [38] implemented in VASP. The local strain introduced by the Li intercalation was fully released by

allowing the free changes in the degrees-of-freedom on atomic positions, the unit cell shape, and cell volume (*e.g.*, no restrictions on the atoms, the symmetry, and the volume) during the full relaxation process. The effect of vdW interactions were considered by employing the semi-empirical correction scheme of Grimme [39-41], implemented in the VASP package (*i.e.*, referred as DFT-D3 in VASP code). The charge transfer between Li and layered phosphorene was evaluated based on the Bader scheme [42-44], which provides an intuitive way of separating the charge related to each atom using first-principles calculations. The charge redistribution in real space was evaluated by the difference of electron charge density (DCD), defined as $\Delta\rho = \rho_{total} - \rho_P - \rho_{Li}$, where ρ_{total} is the total electron charge density of the combined system, ρ_P and ρ_{Li} are the electron charge densities associated with the layered phosphorene (or phosphorus) and Li atoms in the combined system, respectively. Namely, ρ_P (ρ_{Li}) was evaluated by removing Li (P) atoms from the relaxed combined system and calculating the density of states without further relaxation. Thus, the DCD tracks the charge transfer to get an idea of what is interacting with what in the system and how strongly they interact.

III. RESULTS AND DISCUSSIONS

A. Preferential Li deposit positions and distributions

In order to understand how the intercalated Li atoms interact with P atoms of black phosphorene and how these Li atoms play the role in structural transition during the intercalation, we studied the energy landscape of the Li adsorption on phosphorene and then determined the preferential Li deposit positions on the black phosphorene. The results are shown in Figure 1 (a). It is found that positions of the Li atom with relatively low adsorption energy are

along the valley in the zigzag direction, and the minimum energy is at the center of the triangular region formed by P-P-P atoms, referred as VH sites. While positions of the Li atom with relatively high energy are located on the top of the ridge along the zigzag direction with the maximum relative energy on the top of P atoms, referred as TA sites. Thus, based on the adsorption energy landscape, Li prefers to stay at the most stable VH site with the optimized vertical distance of 2.53 Å and the shortest Li-P distance of ~ 2.48/2.66 Å (as shown in Figure 1 (b)), which are within the Li-P bond length of ~ 2.6 Å [45]. It might also possibly stay at the metastable VB and TB sites (*i.e.*, on the top of the middle of P-P bonds) when the most stable VH sites are occupied. Furthermore, since the energy difference along the zigzag direction in the valley (~ 0.1 eV) is much smaller than that along the armchair direction (~ 0.58-0.78 eV), the preferential diffusion path for Li atoms will be easily along the zigzag direction in the valley (see the detail discussion in Ref. [46]). Experimentally, Li intercalation could be carried out either electrochemically or by means of the thermal assisted vapor phase. Various Li distributions on the adsorption energy landscape (*e.g.*, on VH, VB, TB, or TA sites) could happen during the Li intercalation. We have systematically studied the Li diffusion/migration with various Li distributions on VH, VB, TB, and TA sites in our previous work and found that those Li distributions can significantly increase the Li capacity for high-performance of Li-ion battery and have no influence on the structure of black phosphorene [46]. In the present work, on the other hand, we will focus on Li intercalation that Li are mainly distributed on the VH sites, which have the lowest adsorption energy and therefore, are the most preferential and stable on the energy landscape. We want to examine whether such low energy Li configurations could affect the structure of black phosphorene and, if yes, what is the role played by Li atoms during such Li intercalation. We consider a 2x2 supercell of black phosphorene as working system and classify

the bond b_1 (~ 2.22 Å) as the zigzag bond and the bond b_2 (~ 2.31 Å) as the armchair bond (as indicated in Figure 1), respectively. Based on the analysis of the energy landscape for Li deposition on the black phosphorene, it is clear that when Li atoms are intercalated, the most possible positions for Li to stay on the black phosphorene are two types of energetically preferential VH sites. One is on the top surface of phosphorene and the other is at the bottom surface of phosphorene, referred as VH (top) and VH (bottom), respectively (see the light and dark grey balls in Figure 1 (a) and (b)). When a group of Li atoms is intercalated to black phosphorene, they will be expected to physically stay at those VH sites. According to such physical intuition, we have conducted a systematical survey for all possible Li distributions on VH sites and found that the distribution of Li on those energetically preferential VH sites can be described in terms of the P-P armchair bond and clarified as three types of Li occupations. The first type of Li occupation corresponds to Li atoms deposited at one end of armchair bonds, either at the top VH sites (like the white dot shown at the top-left area of the 2x2 super cell in Figure 1 (a)) or at the bottom VH sites (like the grey dot shown at the top-left area of the 2x2 super cell in Figure 1 (a)). The second type of Li occupation corresponds to Li atoms deposited at two ends of armchair bonds, one at the top VH site and the other at the bottom VH site, referring as Li pair (like the grey and white dots shown at the top-right area of the 2x2 super cell in Figure 1 (a)). The third type of Li occupation corresponds to Li atoms deposited on top/bottom VH and top/bottom TH sites (the center of the triangular region formed by P-P-P atoms on the ridge) which will happens when the Li concentration is high (*e.g.*, $n \geq 8$ in Li_nP_{16}). Figure 1 (c)-(e) illustrate these three types of Li occupation. For example, in the first type (*e.g.* config. 1 in Li_8P_{16} shown in Figure S1 [47]), eight Li atoms are distributed alternatively at the top and bottom VH sites on one end of armchair bonds along the zigzag valley (*e.g.*, see the top and side

views on Figure 1 (c)). In the second type (*e.g.*, config. 3 in Li_8P_{16} shown in Figure S1 [47]), eight Li atoms are distributed on both ends of armchair bonds on the left bank of zigzag valleys, one is at the top VH site and the other is at the bottom VH site, forming a Li 'pair' (*e.g.*, see the top and side views on Figure 1 (d)). In the third type (*e.g.* config. 1 in $Li_{16}P_{16}$ in Figure S1 [47]), sixteen Li atoms are distributed at all possible top/bottom VH and TH sites, as shown on the top and side views of Figure 1 (e). Noted that such configuration only exists at high Li concentrations. Other initial Li distributions are different kinds of the mixture of these three types of configurations (see Figure S1 [47]).

B. Li intercalation on phosphorene (Li_nP_{16})

To seek all the possible Li intercalation distributions that guide a transition from black to blue phosphorene, we conducted a systematic survey on Li_nP_{16} systems. For each given Li concentration (*i.e.*, for a given n Li atoms), we considered all possible initial Li configurations that allow intercalated Li atoms deposited on the most energetically preferential VH sites determined from the energy landscape (see Figure S1 [47]). We performed full structural relaxation processes for each configuration using the Conjugate-Gradient algorithm and allowed all atoms moving freely to reach their new equilibrium positions, without any restriction exerted on the shape and the volume of the supercell throughout the relaxation processes so that the local strains induced by intercalated Li atoms can be fully released. In such way, all the considered combined systems were fully relaxed and stabilized (*e.g.*, Figure S2 [47]). We have found out that for a certain Li concentration (*i.e.,* $6 \leq n \leq 16$), the combined systems with all considered configurations reach to three types of stabilized structures: either with no structural transition (referred as no-transition), or with structural transition (referred as transition), or with total or partial bonds breaking (referred as bond-break). Significantly, among those stabilized combined

systems, the most energetically preferential structures are found to be these with the structural transition (see each panel in Figure S2 [47]). To illustrate how the Li intercalation lead to these three types of stabilized structures, we presented in Figure 2 the optimized combined systems of Li_8P_{16} and $Li_{16}P_{16}$ which are fully relaxed starting from the three typical Li configurations (as shown in Figure 1 (c)-(e)).

It was found that the Li intercalation with the first type of the Li configuration does not influence the orthorhombic bone structure of black phosphorene (Figure 2 (a)), indicating that the local strain induced by Li intercalation was very small and only slightly stretched the b_1 and b_2 by about 0.05-0.1 Å. With the second type of the Li configuration, however, the black phosphorene is stabilized to a new structure with a series of six-membered rings linked in trans-decalin fashion (see Figure 2 (b)). Interestingly, this stabilized structure is about 0.2 eV/atom lower in energy than the stabilized structure with the first type of the Li configuration, indicating that for a given composition $n = 8$ (in Li_nP_{16}), the second type of the Li distribution is the most energetically preferential for Li intercalation on phosphorene. Similar trend was also found in other Li_nP_{16} systems with $6 \leq n \leq 16$ (see details in Figure S2 [47]), showing the robustness of our finding. The combined system $Li_{16}P_{16}$ with the third type of the Li configuration, on the other hand, was finally stabilized to an irregular structure with all armchair bonds broken, forming buckled zigzag chains (see Figure 2 (c)). As we found recently, such broken bonds can be self-reformed after removing Li atoms and black phosphorene could self-recover (see Figure 11 in Ref. [46]). We also found that this relaxed structure is energetically higher than the transition structure in $Li_{16}P_{16}$ system (see the config. 2 in the last panel in Figure S2 [47])

What attracts our attention from the above results is the optimized transition structure resulted from the second type of the Li configuration. To understand how this new structure formed and

what the underlying physics is, it is interesting to see whether such structure transition cab be reached starting from the optimized Li_8P_{16} with the first type Li configuration and what happened during the structure transition process. We applied the climbing image nudged elastic band (cNEB) method [48, 49] and studied such structural transition process starting from the optimized structure with no transition (*i.e.*, Figure 2 (a)) to the optimized structure with transition (*i.e.*, Figure 2 (b)). We examined several reaction paths (*e.g.*, see Figure S3 [47]) and found that the minimum energy path (as illustrated in Figure 3) is the reaction path that Li atoms, starting from the first type of the Li configuration, migrate along the zigzag valley and reach the second type of the Li configuration at stage 7 (indicated by the image in Figure 3). Then, they gradually induce a structural deformation on the black phosphorene and finally lead to a series of six-membered rings linked in trans-decalin fashion forms (shown by the insert at the bottom of Figure 3). Estimated reaction energy barrier is ~ 0.1 eV per Li atom, which is equivalent to the lowest Li diffusion barrier along the zigzag valley determined from the Li adsorption energy landscape (see Figure 1 and Figure 4 in Ref. [46]). This low energy barrier indicates that such structural transformation can be easily realized experimentally mediated by Li intercalation.

By examining the structural transition along the minimum energy path (see the snapshots of Figure 4), we also found that armchair bonds with Li pairs located on their both ends are broken at ~ stage 8 (as shown on Figure 4 (b)). Because of such bonds broken, the orthorhombic scaffolding structure is separated into several pieces. Then, pulled by Li atoms, P atoms at the edges of these pieces move up and down, followed by a slowly vertical rotation and vibration. Finally, the intercalated system is stabilized to a series of parallel-arranged buckled rhombohedral-like strips (referred as buckled rhombohedral nanoribbons here after) with Li atoms intercalated between them (Figure 4 (c)). Most interestingly, when we remove Li atoms at

this stage and let the 'broken' black phosphorene undergo a fully relaxation with a periodic condition, surprisingly, few layers of blue phosphorene flakes emerge with P-P bond length of 2.28-2.32 Å and buckling of 1.512 Å (Figure 4 (d)). This result indicates that the inserted Li atoms located on both ends of armchair bonds could act as 'catalysts' and create driving forces to break these armchair bonds, subsequently, the black phosphorene is converted to layered blue phosphorene flakes. Thus, a phase transition from black phosphorene to blue phosphorene can be reached through Li intercalation.

C. The transition mechanism under the Li intercalation

The mechanism of the phase transition from orthorhombic black phosphorus to rhombohedra blue phosphorus under pressure has been pointed out to be an intrinsic reactivity given by lone pairs [15] of P atoms leading to rapid P-P bonds flipping sequences along [001] direction. It is expected that the lone pair rearrangement mechanisms and bond-flipping pattern are geared together, which allows for both the formation of a one-dimensional chain (called Peierls intermediate) and the conservation of lone pair identities. The novel picture of structural transition mechanism induced by Li intercalation without pressure, on the other hand, is expected to be directly related to the interaction between Li and P atoms, or more specifically, hybridization between Li *s* electrons and P lone pairs. As we can see from above results with the second type of the Li configuration (Figure 4), it took two processes accomplishing the phase transition from black to blue phosphorene: the lithiation and the delithiation processes. During the lithiation process, intercalated Li atoms at both ends of armchair bonds (*i.e.*, the Li pairs) act as 'catalysts' and drive the P atoms connecting armchair bonds to move oppositely, resulting in a bond breaking, and subsequently, an assembly of buckled rhombohedral nanoribbons is formed. In the second process, such assembly of buckled rhombohedral nanoribbons are self-mended,

forming buckled rhombohedral layers, and a transition from black to blue phosphorene is reached. Therefore, the Li atoms should play a key role during the intercalation through interacting with P atoms. To better capture such transition mechanism, in particular, to understand how the *s*-like orbitals around Li and *p*-like orbitals around P atoms are hybridized, we performed the electronic charge distribution analysis, in terms of the net electron charges redistribution, especially at the 'reactive centers', and the charges transfer between Li and P atoms associated with the local structural changes during the Li intercalation process, since they are involved in the structural transition and are expected to play active roles during Li intercalation. The real space distribution of the electronic charge density of black phosphorene at the top valence band and the bottom of conduction band are presented in Figure S4 [47]. It is found that the charge density associated with the top valence band is around the lone pairs located outwards of P atoms, as shown in Figure S4 (a) [47], which implies that those lone pairs are chemically active, tend to bond with Li atoms, and will act as 'reactive centers' during Li intercalation. Such interaction/bonding process can be further confirmed from analyzing the net electron charge redistribution of combined Li_nP_{16} systems during the Li intercalation from the difference of electron charge density (DCD) calculations.

Figure 5 depicted some examples of the net electron charge redistribution (DCD) during Li intercalation for combined systems of Li_8P_{16} and $Li_{16}P_{16}$ with three optimized structures, *i.e.*, no-transition, transition, and bond-break, respectively, where the yellow represents the regions of the electron accumulation and the blue represents the regions of electron depletion, respectively. It is found that, for all three types of Li distributions, most net electrons are accumulated between Li and nearby P atoms, and a few electrons are depleted in the regions of lone pairs of P atoms (see the yellow and blue regions in the middle panels of Figure 5 (a)-(c)), demonstrating a strong

hybridization between *s*-like orbitals around Li atoms and *p*-like orbitals associated with the lone pairs of nearby P atoms. Such hybridization pattern, however, depends on the type of the Li distribution and results in different types of final stabilized states after fully relaxation processes. For the combined system with the first type of the Li configuration (*e.g.*, the top panel of Figure 5 (a)), net electrons initially accumulate between Li atoms and P atoms on one end of armchair bonds (indicated by the red dashed circles on Figure 5 (a)), forming Li-P covalent bonds. Such accumulation pattern has no bond breaking effect on armchair bonds, and the black phosphorene in the combined system maintains its orthorhombic structure during such Li intercalation, which can be confirmed by comparing the DCD between the initial and the final stabilized states (*i.e.*, the middle and the bottom panels of Figure 5 (a)). While, for the combined system with the second type of the Li configuration (*e.g.*, the top panel of Figure 5 (b)), net electrons accumulate between Li and P atoms on both ends of alternative armchair bonds (indicated by the red dashed circles on the top and middle panels of Figure 5 (b)), forming two Li-P bonds at both ends of P-P armchair bonds. Such accumulation pattern leads to a P-P bond breaking along the vertical direction, and the combined system is finally stabilized to a new structure with buckled rhombohedral nanoribbons. For the combined system with the third type of the Li configuration, on the other hand, for instance $Li_{16}P_{16}$ (see the top part of Figure 5 (c)), the results of DCD demonstrate that net electron density initially accumulates between all Li and P atoms, forming Li-P bonds (see the red circles on Figure 5 (c)) at both side of all armchair bonds. Thus, the hybridization and the local strain induced by Li intercalation will generate strong stretch on all armchair bonds and totally break them. The combined system is finally stabilized to a broken structure with a series zigzag chains (formed by zigzag bonds) in parallel (see the bottom in

Figure 2 (c)). The net electrons finally accumulate between Li and zigzag chains (see the bottom panel of Figure 5 (c)).

To shed light into the underlying physics of the P-P bond breaking and the structural transition in the second type of Li configuration, we further studied the redistribution of the net electrons accumulation (*i.e.*, the DCD) during the structural transition process (as shown in Figure 3) to track the charge transfer and to understand how Li atoms interact with P atoms in the combined system. The results were presented in Figure 5 (d), where a Li pair at the two ends of an armchair bond (b_2) is denoted by numbers 1 and 2. We found that the electron accumulations between the Li pair and the lone pairs of the two P atoms (indicated by the red-dashed circles at the stage 7) start to spread, and simultaneously, some new accumulations appear at the other sides of the two P atoms of the armchair bonds (*e.g.*, indicated by the black-dashed circles at the stage 8). Such redistribution of the net electron accumulations created a stretch in the armchair bonds in a very short time and leaded to armchair bonds broken (*e.g.*, indicated by the red-dashed line at the stage 8). The black phosphorene layer was then broken down to pieces of nanoribbons. In the following reaction stages (see the stage 10 and the final stage in Figure 5 (d)), the local strain associated with the bond breaking and the Li intercalation further drove the redistributions of the net electron accumulations and the reorientation of the lone pairs, accompanied by the redistribution of the Li atoms (*e.g.*, indicated by the red-dashed circles and black arrows at the stage 10 and the final stage), leading to a rotation of the nanoribbons, until the local strain was fully released. At the final stage, net electron density re-accumulates between Li atoms and new lone pairs of P atoms of adjacent buckled rhombohedral nanoribbons (indicated by the black-dashed circles at the final stage in Figure 5(d)).

Our Bader analysis pointed out that for the combined system of Li_8P_{16} with the first type of the Li configuration, the charge transfers between Li and P atoms keep 0.804*e*/Li and -0.402*e*/P before and after relaxation process, confirming that such Li distribution will not affect the structure of black phosphorene (as shown in Figure 2 (a) and Figure 5 (a)). For the combined system of Li_8P_{16} with the second type of the Li configuration, the charge transfers between Li ad P atoms are 0.798*e*/Li and -0.399*e*/P at the initial state, and 0.824*e*/Li and -0.412*e*/P at the final state. The increase in charge transfer during relaxation process demonstrates that such Li distribution can affect the structure of black phosphorene and lead to a structure transformation via hybridization between *s*-like orbitals around Li atoms and *p*-like orbitals around lone pair of P atoms (as shown in Figure 2 (b) and Figure 5 (b) and (d)). For the combined system of $Li_{16}P_{16}$ with the third type of the Li configuration, on the other hand, the charge transfers between Li ad P atoms keep symmetric nature during the whole relaxation process, *i.e.*, 0.544*e*/Li and -0.544*e*/P at the initial state, and 0.764*e*/Li and -0.764*e*/P at the final state. The change in charge transfer during such relaxation process shows that this Li distribution can break the structure of black phosphorene to a series of zigzag chains via hybridization. The distribution symmetry of the charge transfer also indicates that the interactions between all Li and P atoms are uniform (as shown in Figure 2 (c) and Figure 5 (c)).

From above analyses of orbital hybridization and electron charge redistribution, we conclude that when a Li pair is intercalated at the both ends of an armchair bond (which is energetically preferential Li distribution as discussed in subsection B), the hybridization between the Li pair and lone pairs of P atoms of such armchair bond could induce the stretch on the bond and lead to such bond breaking and a decomposition of the black phosphorene. Local strain accompanied with intercalated Li atoms played the key role in stabilizing the decomposed system through the

reorientation of the lone pairs and the rotation of the decomposed structures. As the results an assembly of buckled rhombohedral nanoribbons is formed and a structure transition is reached without the instable Peierls intermediate found in the pressure induced phase transition [15]. Namely, the lone pairs of P atoms play as a 'reactive centers', and the Li pair plays as a 'catalyst' triggering the armchair bonds breaking. In particular, when such armchair bonds are on the same side of the zigzag valley, a series of buckled rhombohedral nanoribbon form after the armchair bonds broken, and these buckled rhombohedral nanoribbons become the building block of blue phosphorene. After removing Li atoms, those nanoribbons are self-mended, subsequently forming a layered blue phosphorene. Thus, the Li intercalation can induce a structure transition from black to blue phosphorene, providing a new possible route for synthesizing blue phosphorene.

D. Identify specific conditions for structure transition

Based on the above atomistic model, we have conducted a comprehensive survey to identify specific conditions for Li_nP_{16} systems such that the inserted Li atoms could induce the structural transformation from black to blue phosphorene. Various Li intercalation rates and distributions for a given rate were considered allowing Li pairs located at the 'reactive centers' (*i.e.*, both sides of armchair bonds). All the combined Li_nP_{16} systems are fully relaxed and corresponding optimized structures were obtained (see Figures S1 and S2 for details [47]). The following combined Li_nP_{16} systems have been identified which can possibly lead to a structural transition from black to blue phosphorene: Li_6P_{16} (with one possible configuration), Li_7P_{16} (with one possible configuration), Li_8P_{16} (with five possible configurations), Li_9P_{16} (with nine possible configurations), $Li_{10}P_{16}$ (with two possible configuration), and $Li_{16}P_{16}$ (with one possible configuration). Figure 6 depicts the dynamic results of some examples for Li_6P_{16}, $Li_{10}P_{16}$, and

$Li_{16}P_{16}$, respectively. It was found that even though the degree of the 'rotation' of parallel-arranged buckled rhombohedral nanoribbons (see middle panels of Figure 6) driven by the local strain depends on the distribution of Li pairs (see left panels of Figure 6), they all can lead to a phase transition from black phosphorene to layers of blue phosphorene after delithiation (right panels of Figure 6). Furthermore, the most possible Li composition among the combined Li_nP_{16} systems is found at n ~9 (with nine possible Li distribution configurations for structural transition), indicating that the phase transition from black to blue phosphorene will most likely happen with the Li concentration of x ~0.56 (*i.e.*, n = 9 in Li_nP_{16}), which provide a useful information/guideline for synthesizing blue phosphorene from black phosphorene by Li intercalation.

Interestingly, in our study on Na and K intercalations, we did not find such structure transformation. Figure 7 shows, as examples, the optimized (right panels) intercalated systems of $Li_{10}P_{16}$, $K_{10}P_{16}$, and $Na_{10}P_{16}$, respectively. Unfortunately, there is no phase transition found even though the K and Na atoms are distributed closely to the 'reactive centers' (left panels of Figure 7 (b) and (c)), following the same Li distribution in $Li_{10}P_{16}$ (left panels of Figure 7 (a)). Optimized structures show that, all K and Na atoms prefer to stay away from black phosphorene surfaces, and none of the armchair bonds is broken, completely different with the case of $Li_{10}P_{16}$ (see right panels of Figure 7). Such results mostly come from their large atomic radius (K ~2.27 Å; Na ~1.86 Å) [50], which lead to their energetically preferential adsorption positions far away from the black phosphorene surface, as compared to Li atoms (*e.g.*, calculated equilibrium distances are ~ 3.36 Å for K-P and 3.00 Å for Na-P, much larger than that of Li-P (~ 2.48-2.66 Å)). Our DCD calculations for these systems (Figure S5 [47]) demonstrated that there are almost no orbital hybridization between K and P atoms (the right panel in Figure S5 (b) [47]), and very

weak hybridization between Na and P atoms (the right panel in Figure S5 (c) [47]), as compared to Li and P atoms (the right panel in Figure S5 (a) [47]). These analyses, therefore, confirmed that the attractive interactions between K (Na) and P atoms are not sufficiently enough to pull P atoms out to break the armchair bonds. But they can be used as good candidates for exfoliating black P. Thus, the fundamental mechanism for the intercalation-induced transition from black to blue phosphorene should be a synergic effect of the orbital hybridization, charge transfer, and the strength of the electrostatic Coulomb interactions between alkali and P atoms. This finding is expected to be validated by experiments.

E. Li intercalation on double layer and multilayer black phosphorene

When Li atoms are intercalated between black phosphorene layers, they will not only interact with P atoms at the bottom surface of upper layer, but also with P atoms at the top surface of the bottom layer. This phenomenon can be seen, for instance, from the DCD analysis on the initial states of double layered $Li_{16}P_{32}$ and multilayered Li_3P_8 (see Figure 8 (a) and (c)). The electron accumulation (the yellow color) appears between Li and P atoms at adjacent layers, mainly due to the orbital hybridization between Li atoms and P atoms at adjacent layers. Therefore, it is expected that the numbers of Li atoms that required to play as 'catalysts' to induce the structural transition from black to blue layered phosphorene could be reduced in the case of layered black phosphorene. Our systematic study has found that the required Li concentration window is $0.375 \leq x \leq 1.0$ (*e.g.*, $6 \leq n \leq 16$ in Li_nP_{16}) for monolayer black phosphorene. While, for double layered black phosphorene, the required Li concentration window is around $0.5 \leq x < 0.625$ (*e.g.*, $16 \leq n \leq 20$ in Li_nP_{32}), and for multilayers or black phosphorus, the required Li concentration window is reduced to the range of $0.375 \leq x < 0.5$ (*e.g.*, $3 \leq n < 4$ in Li_nP_8).

The Li intercalation-induced structural transition processes for double layered $Li_{16}P_{32}$ (or $Li_{0.5}P$) with AA stacking and multilayered Li_3P_8 (or $Li_{0.375}P$) with AB stacking are presented in Figure 8, as two distinguished examples. In both cases, following the atomistic model developed in subsection C, all Li atoms are deposited at top and bottom VH sites, which are either on one side or both sides of armchair bonds (*e.g.*, see top views in Figure 9 (a) and (d)). Similarly, it was found that during the lithiation process, Li atoms hybridize P atoms at both ends of armchair bonds and induce armchair bonds breaking, and then an assembly of buckled rhombohedral nanoribbons formation associated with the release of the local strain (*e.g.*, see Figure 9 (b) and (e)). Next, when Li atoms were removed, the assembly of these nanoribbons are self-mended to release the local strains during the delithiation process, and finally form blue phosphorene layers (see Figure 9 (c) and (f)). One of the most interesting findings is that, induced by Li intercalation, the double layered black phosphorene with AA stacking (see the top view of Figure 9 (a)) was converted to a layered blue phosphorene with AA stacking (see the top view of Figure 9 (c)), while, multilayered black phosphorene with AB stacking (see the top view of Figure 9 (d)) was converted to multilayered blue phosphorene with ABC stacking (see the right panel of Figure 9 (f), which was also found experimentally under high pressure [28]) since the Li intercalation leads to an antisymmetric distribution of buckled rhombohedral nanoribbons between layers (Figure 9 (e)). The equilibrium interlayer distance (d) is found ~4.60 Å for double layer blue phosphorene with AA stacking and ~4.13 Å for multilayer blue phosphorene with ABC stacking, indicating a stacking/layer dependent vdW weak interaction between layers. Thus, it is possible to peal out a monolayer by mechanical exfoliation. Furthermore, these results also confirm our assumption that the more the number of layers, the less the Li atoms required triggering a structural transition. Thus, the conditions for Li distribution to induce a phase transition from

black to blue phosphorene will also depend on the number of layers and therefore provide a fundamental guide for fabricating blue phosphorene by using this novel kinetic growth pathway.

IV. CONCLLUSION

Our systematic study on different Li_xP_{1-x} structures (including mono-, double-, and multi-layer black phosphorene) and various Li distributions (over fifty configurations), as well as their energies predicted that at sufficiently high Li concentration and certain well-defined configurations a phase transition from black to blue phosphorene can occur. Such finding was further confirmed by careful evaluations using the full-electron PAW potential for Li and extending the supercell from 2x2 to 4x4 (see Figure S6 for details [47]). The precise atomistic picture and the evidence of a phase transition from black phosphorene to blue phosphorene are demonstrated in terms of (1) the hybridization between *s*-like orbitals located around Li atoms and *p*-like orbitals located around the lone pair of P atoms on both ends of armchair bonds, leading to such bond breaking and (2) the release of the local strains induced by Li intercalation and bond breaking, leading to the reorientation of the lone pairs and rearrangement of the decomposed system. Subsequently, the puckered orthorhombic structure of black phosphorene converts to an assembly of buckled rhombohedral nanoribbons. Thus, Li atoms located at these 'reactive centers' (near the lone pairs of P atoms of P-P armchair bonds) act as 'catalysts' to trigger the structural transition from black to layered blue phosphorene. The conditions to realize such phase transition through Li intercalation are identified, and the required Li concentration is $0.375 < x \leq 1.0$ for monolayer phosphorene, $0.5 \leq x < 0.625$ for double layered phosphorene, and $0.375 \leq x < 0.5$ for black phosphorus, respectively. Along this way, the insight into the fundamental information at atomic level for fabricating/growing blue phosphorene was provided.

It should be noted that the orientation of the blue phosphorene nanoribbons with respect to the pristine black phosphorene depends on the local strain induced by Li intercalation, and the effect of such local strain depends on the Li concentration, the Li distribution, and the number of black phosphorene layers (*e.g.*, ~90^0 in Li_8L_{16} and $Li_{16}P_{16}$ monolayer and $Li_{16}P_{32}$ bi-layer, but ~ 45^0 in $Li_{10}L_{16}$ monolayer and Li_3P_8 in multilayer, respectively). As the results, the monolayer or bilayer black phosphorene could be transformed to an assembly of nanoribbons of blue phosphorene or flakes. The size of the layered blue phosphorene flakes depends on the number of black phosphorene layers. The more, the layers, the larger the size. Practically, multilayered black phosphorus is a good candidate to obtain layered blue phosphorus. The Li interaction, delithiation, and controlling the Li concentration can be realized in experiment, for example, through electrochemical Li charging/discharging technique within a controlled voltage window. Furthermore, from new experimental reports on the phases transition from black to blue phosphorus under pressure [28], it is known that experimentally identifying such phase transition or the co-existence of black and blue phosphorus can be realized from the change of the slops of Raman shift on B_{2g} and A_{2g} modes within a small range of the frequency (*e.g.,* ~ 6 cm^{-1}). Thus, one needs to fine-tune in such measurement to dig out the details in a tiny range with a small change, which might reflect a structural transition. Our work is the first report on the intercalation-induced phase transition in a layered material system. Although this is a vastly unexplored area, our study points out the possibility of other systems, where intercalation can lead to an unexpected bond restructuring, structural phase transitions, and can even lead to the discovery of novel materials.

ACKNOWLEDGMENT

This work is supported by the U.S. Department of Energy, Office of Science, Basic Energy Sciences, under Award # DE-SC0019348. M. R. K. Musa, C.Y. Zhang, and M. Yu are grateful for the computing resource support from the Cardinal Research Cluster at the University of Louisville

REFERENCES

[1] K. S. Novoselov, A. K. Geim1, S. V. Morozov, D. Jiang, Y. Zhang, S. V. Dubonos, I. V. Grigorieva1, and A. A. Firsov, Science **306**, 666-669 (2004).

[2] C. Lee, X. D. Wei, J. W. Kysar, and J. Hone, Science **321**, 385-388 (2008).

[3] Aron W. Cummings, Dinh Loc Duong, Van Luan Nguyen, Dinh Van Tuan, Jani Kotakoski, Jose Eduardo Barrios Vargas, Young Hee Lee, and Stephan Roche, Advanced Materials **26**, 5079-5094 (2014)

[4] M. Singh, H. M. Haverinen, P. Dhagat, and G. E. Jabbour, Advanced Materials **22**, 673-685 (2010).

[5] P. A. Hu, Z. Z. Wen, L. F. Wang, P. H. Tan, and K. Xiao, ACS Nano **6**, 5988-5994 (2012).

[6] T. C. Niu and A. Li, Progress in Surface Science **90**, 21-45 (2015).

[7] Meysam Akhtar, George Anderson, Rong Zhao, Adel Alruqi, Joanna E. Mroczkowska, Gamini Sumanasekera, and Jacek B. Jasinski, npj 2D Materials and Applications **1**, 5 (2017).

[8] A. S. Rodin, A. Carvalho, and A. H. Castro Neto, Phys. Rev. Letters **112**, 176801 (2014).

[9] Andres Castellanos-Gomez, Leonardo Vicarelli, Elsa Prada, Joshua O Island, K L Narasimha-Acharya, Sofya I Blanter, Dirk J Groenendijk, Michele Buscema, Gary A Steele, and J V Alvarez, 2D Materials **1**, 025001 (2014).

[10] Etienne Gaufrès, Frédéric Fossard, Vincent Gosselin, Lorenzo Sponza, Franc□ois Ducastelle, Zhenglu Li, Steven G. Louie, Richard Martel, Michel Co□té, and Annick Loiseau, Nano Lett. 19, 8303−8310 (2019).

[11] G.-C. Guo, X.-L. Wei, D. Wang, Y. Luo, and L.-M. Liu, J. of Mater. Chem. A **3,** 11246-11252 (2015).

[12] Han Liu, Adam T. Neal, Zhen Zhu, Zhe Luo, Xianfan Xu, David Tománek, and Peide D. Ye, ACS Nano **8**, 4033-4041 (2014).

[13] Shuang Zhang, Jiong Yang, Renjing Xu, Fan Wang, Weifeng Li, Muhammad Ghufran, Yong-Wei Zhang, Zongfu Yu, Gang Zhang, Qinghua Qin, and Yuerui Lu, ACS Nano **8**, 9590-9596 (2014).

[14] Z. Zhu and D. Tománek, Phys. Rev. Letters **112**, 176802 (2014).

[15] S. E. Boulfelfel, G. Seifert, Y. Grin, and S. Leoni, Phys. Rev. B **85**, 014110 (2012).

[16] J.-J. Zhang and S. Dong, 2D Materials **3**, 035006 (2016).

[17] Jiafeng Xie, M. S. Si, D. Z. Yang, Z. Y. Zhang, and D. S. Xue, J. of Appl. Phys. **116**, 073704 (2014).

[18] Tao Hu and Jisang Hong, J. of Appl. Physics **118**, 054301 (2015).

[19] Ram Swaroop, P. K. Ahluwalia, K. Tankeshwar, and Ashok Kumar, RSC Adv. **7**, 2992–3002 (2017).

[20] Liyan Zhu, Shan-Shan Wang, Shan Guan, Ying Liu, Tingting Zhang, Guibin Chen, and Shengyuan A. Yang, Nano Lett. **16**, 6548−6554 (2016).

[21] Jia Lin Zhang, Songtao Zhao, Cheng Han, Zhunzhun Wang, Shu Zhong, Shuo Sun, Rui Guo,Xiong Zhou, Cheng Ding Gu, Kai Di Yuan, Zhenyu Li, and Wei Chen, Nano Lett. **16**, 4903−4908 (2016).

[22] Chengding Gu, Songtao Zhao, Jia Lin Zhang, Shuo Sun, Kaidi Yuan, Zehua Hu, Cheng Han, Zhirui Ma, Li Wang, Fengwei Huo, Wei Huang, Zhenyu Li, and Wei Chen, ACS Nano **11**, 4943−4949 (2017).

[23] Jincheng Zhuang, Chen Liu, Qian Gao,| Yani Liu, Haifeng Feng, Xun Xu, Jiaou Wang, Jijun Zhao, Shi Xue Dou, Zhenpeng Hu,| and Yi Du, ACS Nano **12**, 5059−5065 (2018).

[24] Jiang Zeng, Ping Cui, and Zhenyu Zhang, Phys. Rev. Lett. **118**, 046101 (2017).

[25] T. Kikegawa and H. Iwasaki, Acta Crystallographica Section B: Structural Science **39**, 158-164 (1983).

[26] J. C. Jamieson, Science **139**, 1291-1292 (1963).

[27] M. Okajima, S. Endo, Y. Akahama, and S.-i. Narita, Jap. J. of Appl. Phys. **23**, 15 (1984).

[28] Anirban Kundu, Damien Tristant, Natalya Sheremetyeva, Anthony Yoshimura, Abraao Torres Dias, Kiran Shankar Hazra, Vincent Meunier, and Pascal Puech, Nano Letters **20**, 5929-5935 (2020).

[29] Dmitriy A. Dikin, Sasha Stankovich, Eric J. Zimney, Richard D. Piner, Geoffrey H. B. Dommett, Guennadi Evmenenko, SonBinh T. Nguyen, and Rodney S. Ruoff, Nature **448**, 457-460 (2007).

[30] Manish Chhowalla, Hyeon Suk Shin, Goki Eda, Lain-Jong Li, Kian Ping Loh, and Hua Zhang, Nature Chemistry **5**, 263-275 (2013).

[31] W. Kohn and L. J.Sham, Phys. Rev. **140**, A1133 (1965).

[32] P. Hohenberg and W. Kohn, Phys. Rev. **136**, B864 (1964).

[33] G. Kresse and J. Furthmüller, Phys. Rev. B **54**, 11169 (1996).

[34] P. E. Blöchl, Phys. Rev. B **50**, 17953 (1994).

[35] J. P. Perdew, J. A. Chevary, S. H. Vosko, K. A. Jackson, M. R. Pederson, D. J. Singh, and C. Fiolhais, Phys. Rev. B **46**, 6671 (1992).

[36] J. P. Perdew, K. Burke, and M. Ernzerhof, Phys. Rev. Letters **77**, 3865 (1996).

[37] H. J. Monkhorst and J. D. Pack, Phys. Rev. B **13**, 5188 (1976).

[38] X. Gonze, Phys. Rev. B **55**, 10337 (1997).

[39] S. Grimme, J. of Comp. Chem. **27**, 1787-1799 (2006).

[40] S. Grimme, J. Antony, S. Ehrlich, and H. Krieg, J. of Chem. Phys. **132**, 154104 (2010).

[41] S. Grimme, S. Ehrlich, and L. Goerigk, J. of Comp. Chem. **32**, 1456-1465 (2011).

[42] Richard F.W. Bader, Chem. Rev. **91**, 893-928 (1991).

[43] W. Tang, E. Sanville, and G. Henkelman, J. of Physics: Condensed Matter **21**, 084204 (2009).

[44] M. Yu and D. R. Trinkle, J. of Chem. Phys. **134**, 064111 (2011).

[45] Q.Y. Shao, G.W. Wang, J. Zhang, and K.G. Zhu, Condensed Matter Physics **16**, 13702 (2013).

[46] C. Zhang, M. Yu, G. Anderson, R. R. Dharmasena, and G. Sumanasekera, Nanotechnology **28**, 075401 (2017).

[47] See Supplemental Material at [URL will be inserted by publisher] for Li intercalations on black phosphorene, electron charge distribution of black phosphorene, and the difference of electron charge density of combined Li_nP_{16}.

[48] G. Henkelman and H. Jónsson, J. Chem. Phys. **113**, 9901-9904 (2000).

[49] G. Henkelman and H. Jónsson, J. Chem. Phys. **113**, 9978-9985 (2000).

[50] Data taken from John Emsley, The Elements, 3rd edition. Oxford: Clarendon Press, https://www.angelo.edu/faculty/kboudrea/periodic/trends_atomicradius.htm (1998**).**

FIGURE CAPTIONS

Figure 1. (a) The adsorption energy landscape of Li atom deposited on black phosphorene. The colors on the left-hand column scale the adsorption energy at an adsorption site relative to that at the VH site. The notations of VH, VB, TB, and TA represent the specific Li adsorption sites, as defined in the text. A schematic structure of the 2×2 phosphorene supercell is inserted to illustrate the Li adsorption positions. The zigzag and armchair bonds are indicated by b_1 and b_2, respectively. (b) Side view of Li atoms deposited on the top and bottom VH sites and the numbers represent the shortest distances between Li and P atoms and the vertical distance. The top (up) and side (bottom) views of initial Li configurations of (c) Li_8P_{16} with the first type of the initial Li configuration, (d) Li_8P_{16} with the second type of the initial Li configuration, and (e) $Li_{16}P_{16}$ with the third type of the initial Li configuration, respectively. The pink balls denote P atoms, and light and dark grey balls represent Li atoms at top and bottom VH sites, respectively.

Figure 2. Three types of optimized structures indicated by the blue arrows and denoted as no-transition, transition, and bond-break, respectively. (a) Li_8P_{16} with the first type of the Li configuration, (b) Li_8P_{16} with the second type of the Li configuration, and (c) $Li_{16}P_{16}$ with the third type of the Li configuration, respectively. The total energy per atom is presented in the parentheses and the side views of the final stabilized structures in (b) and (c) are guided by the arrows. The pink and light grey balls denote P and Li atoms, respectively.

Figure 3 The reaction energy per Li atoms along the structural deformation/reaction path starting from the optimized Li_8P_{16} with the first type of the Li configuration (*i.e.*, the structure

shown at the bottom of Figure 2 (a)), and ending to the optimized transition structure of Li_8P_{16} with the second type of the Li configuration (*i.e.*, the structure shown at the bottom of Figure 2 (b)). The image shows the Li migration (indicated by a series of light grey balls) along the zigzag valley during the first half of the reaction path with the energy barrier of ~ 0.1 eV. The inserts show the structures at the stage 7 (top) and the final stage (bottom), respectively.

Figure 4. Snapshots of Li_8P_{16} during lithiation ((a)-(c), *i.e.*, stages along the reaction path shown in Figure 3) and delithiation (d) processes. P and Li atoms are presented by pink and light grey balls, respectively.

Figure 5. Top views of initial configurations (top panels), DCD of initial states (middle panels), and DCD of final states (bottom panels) for (a) Li_8P_{16} with the first type of the initial Li configuration, (b) Li_8P_{16} with the second type of the initial Li configuration, and (c) $Li_{16}P_{16}$ with the third type of the initial Li configuration, respectively. (d) The snapshots of DCD for Li_8P_{16} (with the second type of the Li configuration) during structural transition process as shown in Figures 3 and 4. The electron accumulation and depletion (at the isosurface of 0.004 e/Å^3) are represented by the yellow and blue colors, respectively. The red dashed circles indicate the hybridization between *s*-like orbital located around Li atoms and *p*-like orbitals around the lone pairs of P atoms. Black arrows point the net electrons accumulate near lone pairs. Pink and light grey balls present P and Li atoms.

Figure 6. Lithiation and delithiation processes of (a) Li_6P_{16}, (b) $Li_{10}P_{16}$, and (c) $Li_{16}P_{16}$, respectively. Pink and light grey balls represent P and Li atoms.

Figure 7. Initial (left) and final (right) states of (a) $Li_{10}P_{16}$, (b) $Ki_{10}P_{16}$, and (c) $Na_{10}P_{16}$, respectively, where pink, blue, and green balls represent P, K, and Na atoms.

Figure 8. DCD at the initial states of (a) the double layer $Li_{16}P_{32}$ with AA stacking and (c) the multilayer Li_3P_8 with AB stacking, respectively. (b) and (d) are DCD at the final states of systems in (a) and (c). The electron accumulation and depletion (at the isosurface of 0.004 e/Å^3) are represented by the yellow and blue colors, respectively. The pink and grey balls represent P and Li atoms, respectively.

Figure 9. (a) Top (up) and side (bottom) views of double layered $Li_{16}P_{32}$ with initial Li configuration. (b) Two side views of stabilized double layered $Li_{16}P_{32}$ after full relaxation. (c) Two side views of stabilized blue phosphorene layers with AA stacking after delithiation. (d) multilayered $Li_{0.375}P$ with initial Li configuration (top and side views) undergoes (e) a structural transition induced by Li intercalation. After removing Li atoms, the system is finally stabilized to (f) blue phosphorus with ABC stacking. The notations of d and Δz are the interlayer distance and buckling, respectively.

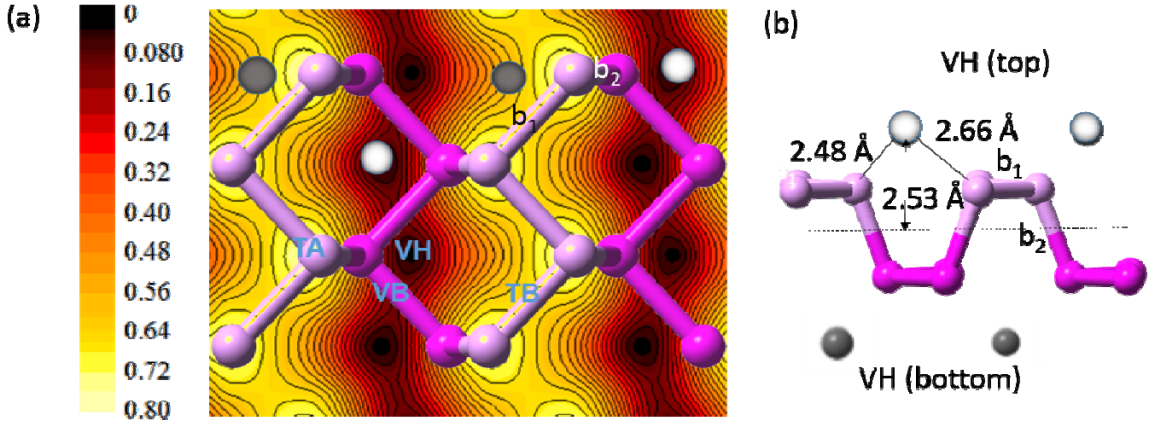

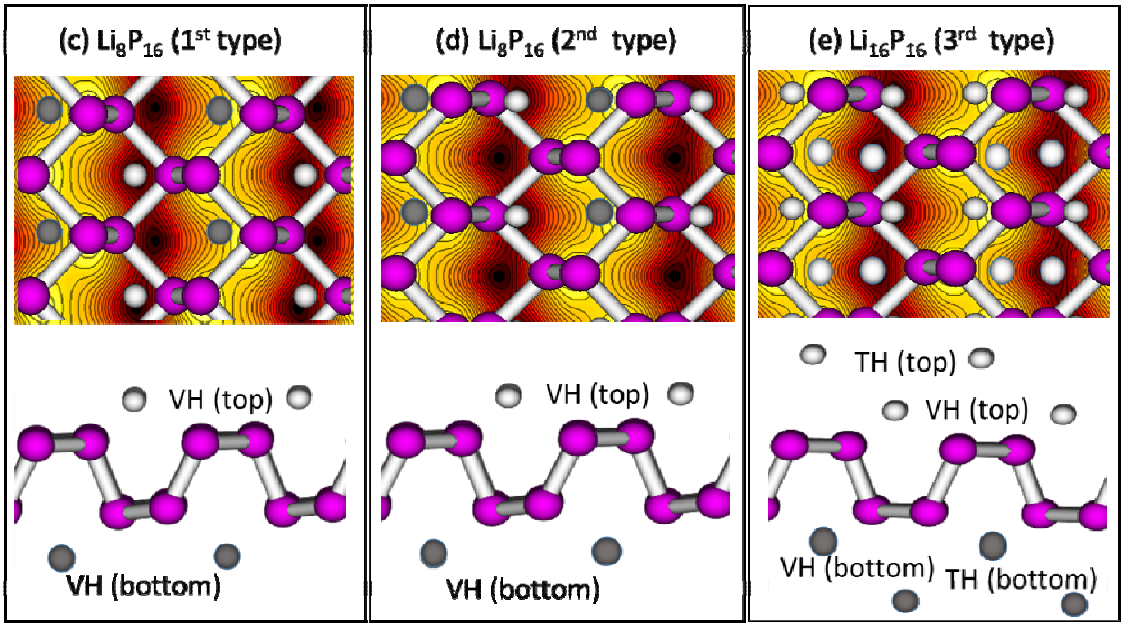
(c) Li_8P_{16} (1st type)
VH (top)
VH (bottom)
(d) Li_8P_{16} (2nd type)
VH (top)
VH (bottom)
(e) $Li_{16}P_{16}$ (3rd type)
TH (top)
VH (top)
VH (bottom)
TH (bottom)

Figure 1

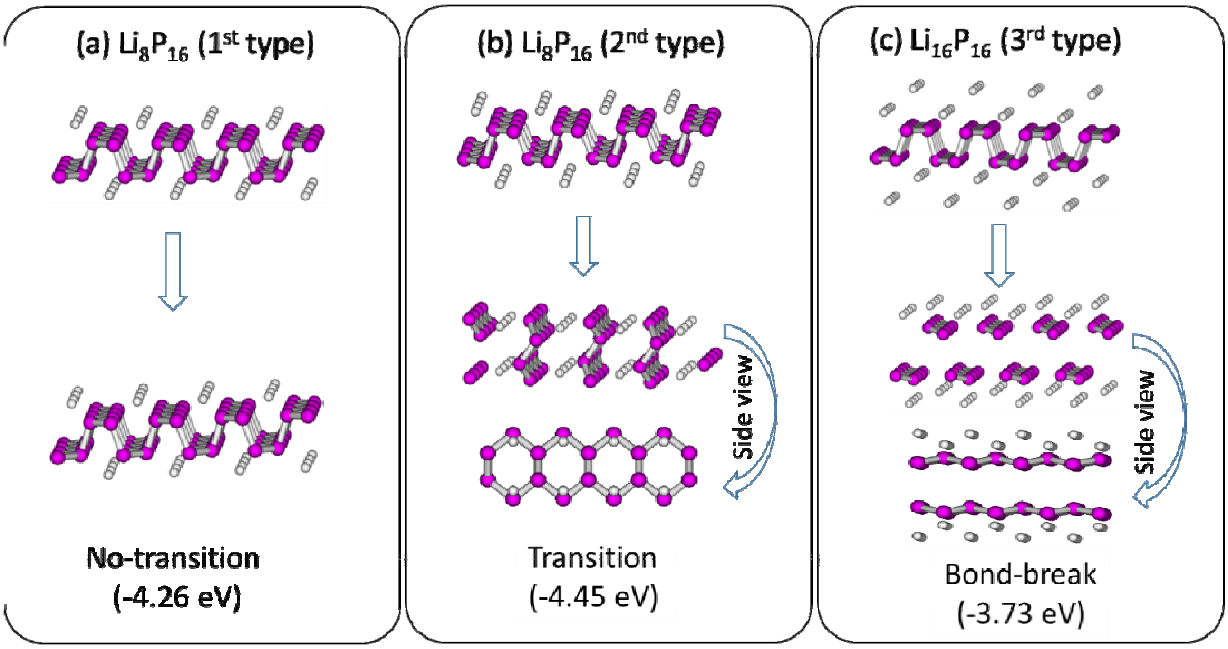

Figure 2

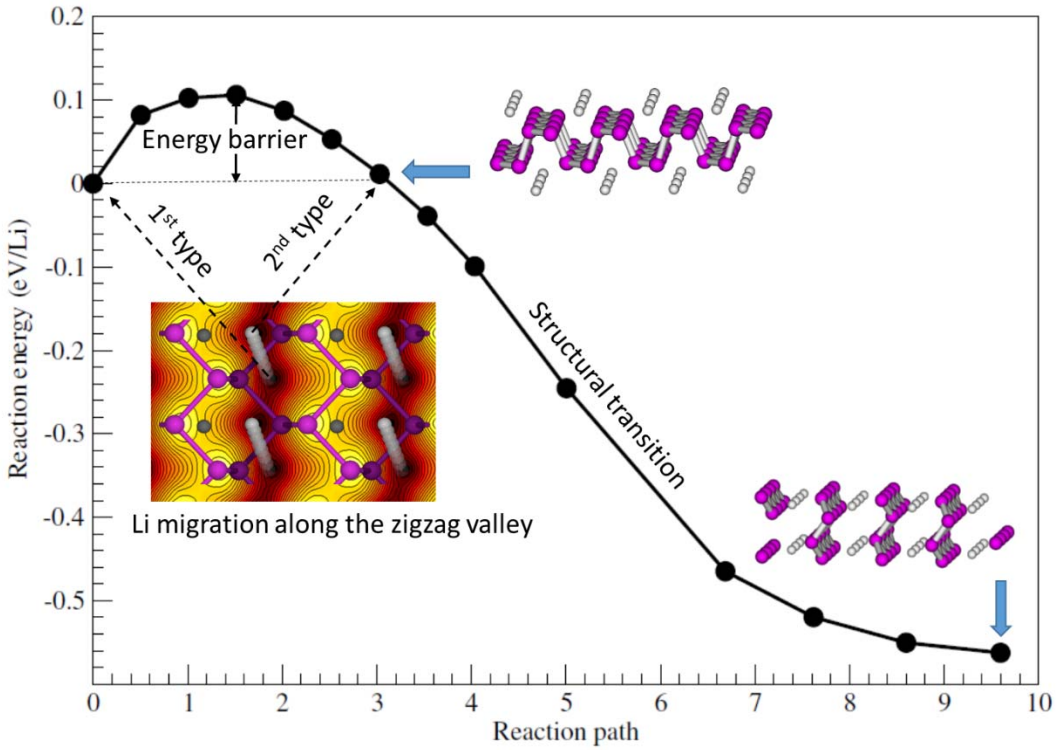

Figure 3

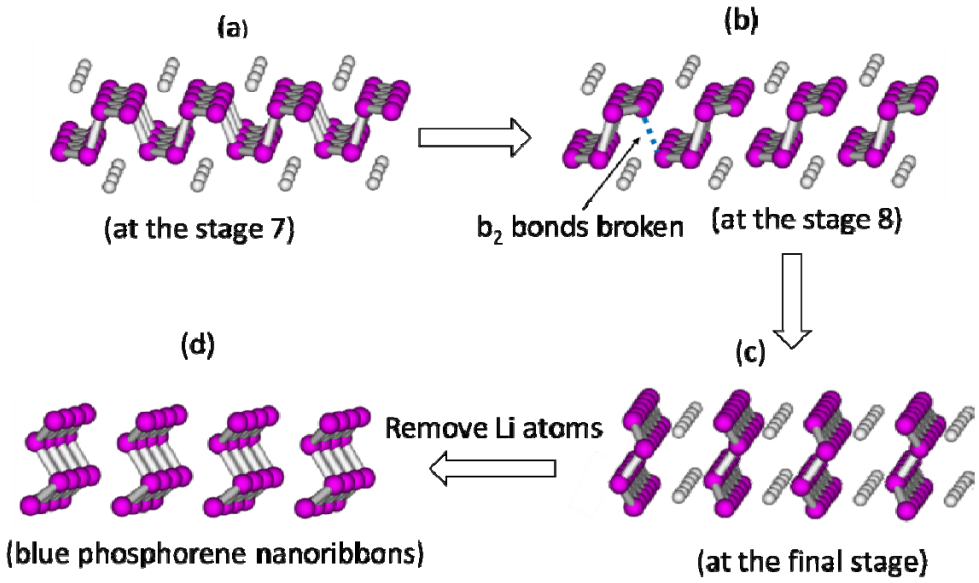
(a)
(b)
(at the stage 7)
b_2 bonds broken
(at the stage 8)
(d)
(c)
Remove Li atoms
(blue phosphorene nanoribbons)
(at the final stage)

Figure 4

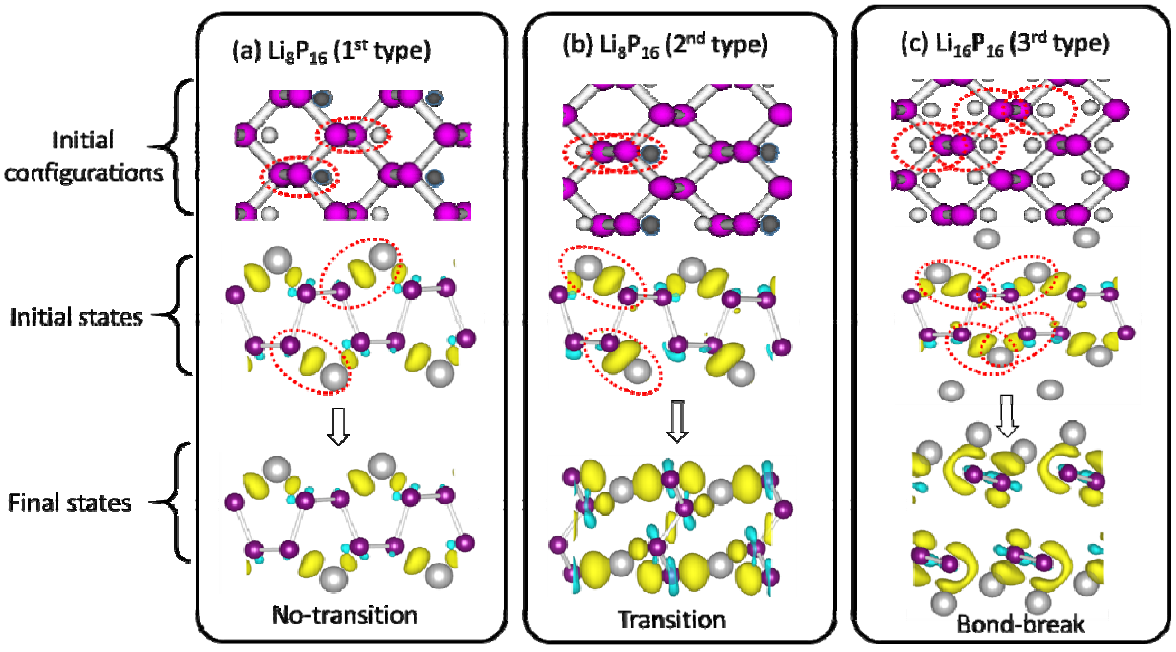
(a) Li_8P_{16} (1st type)
(b) Li_8P_{16} (2nd type)
(c) $Li_{16}P_{16}$ (3rd type)
Initial configurations
Initial states
Final states
No-transition
Transition
Bond-break

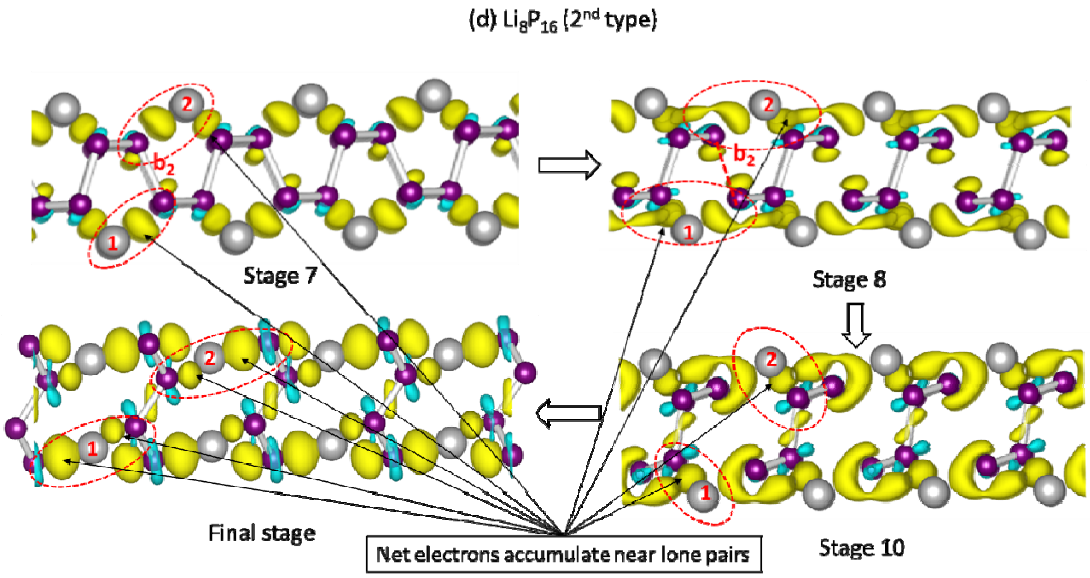

Figure 5

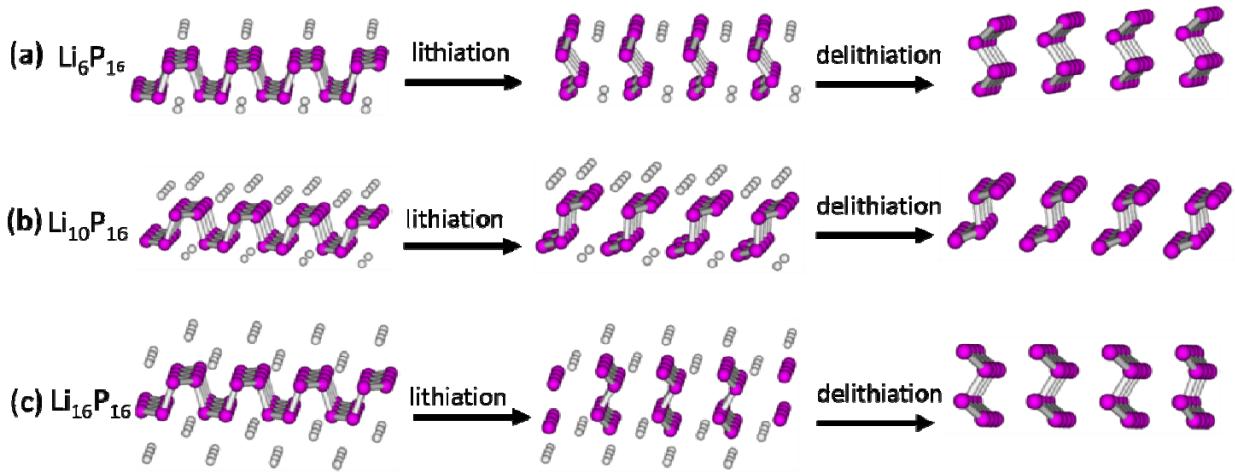

Figure 6

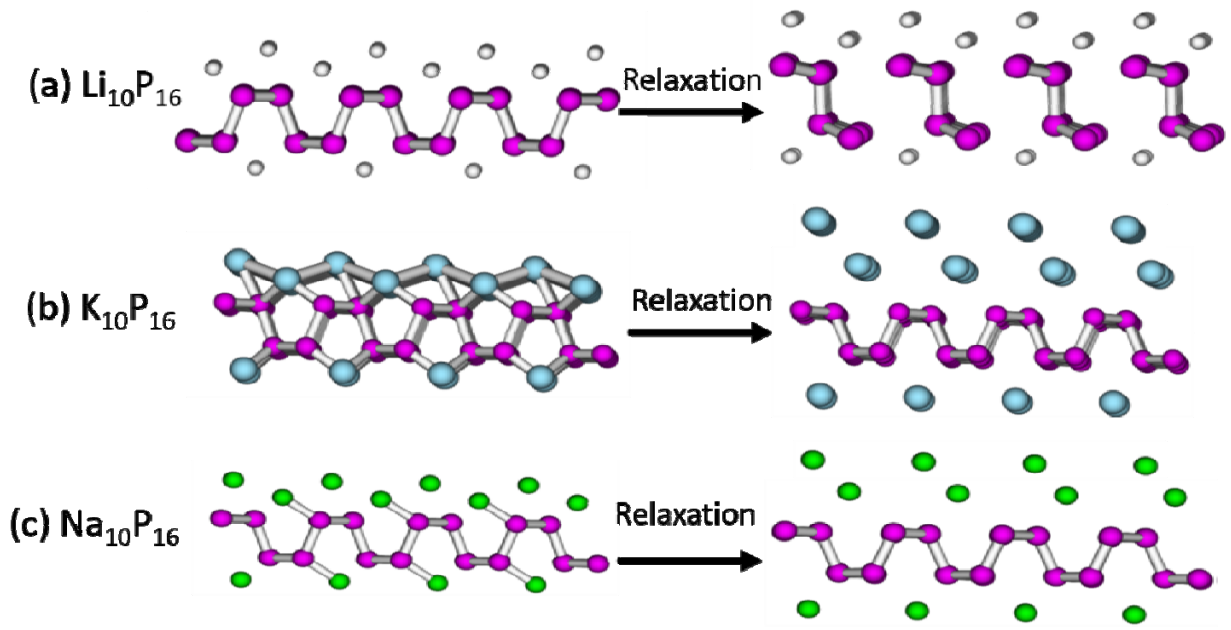

Figure 7

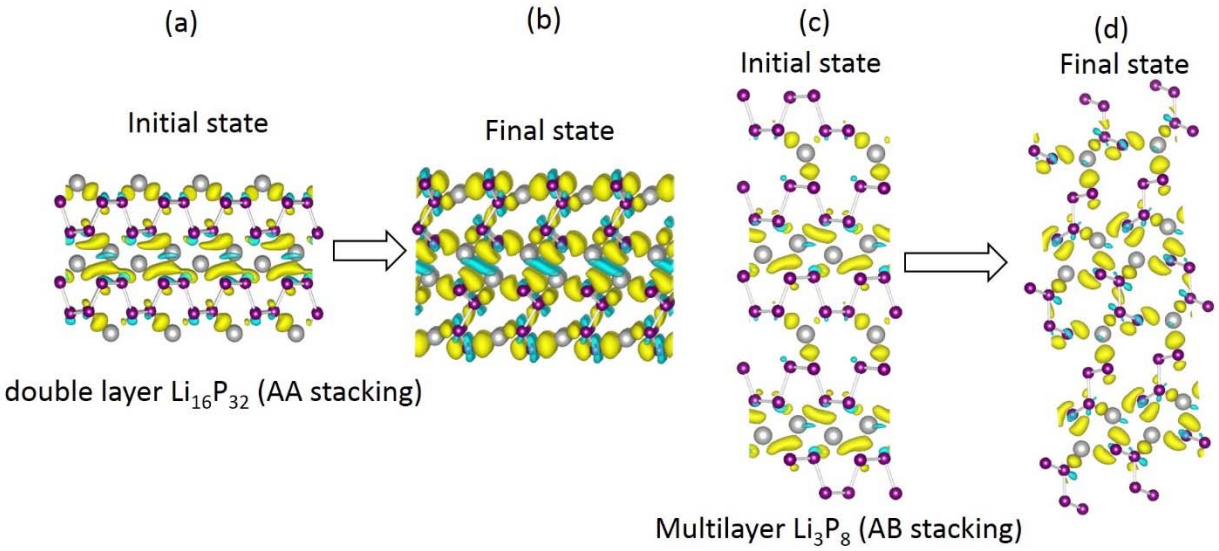

Figure 8

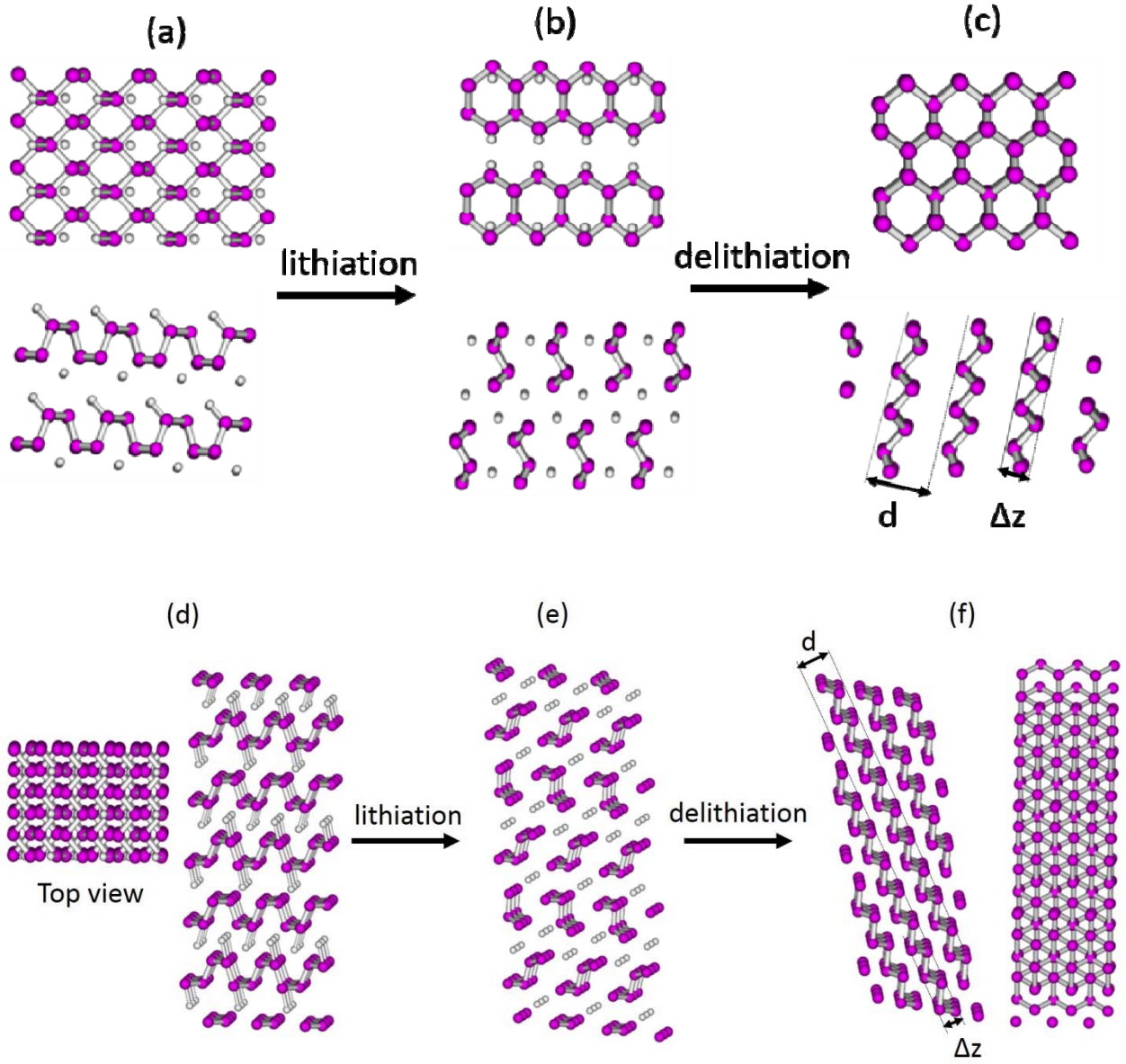
(a)
(b)
(c)
lithiation
delithiation
d
Δz
(d)
(e)
(f)
Top view
lithiation
delithiation
d
Δz

Figure 9